Journal of Geophysical Research: Planets

RESEARCH ARTICLE
10.1029/2018JE005750

The Impact of Comet Siding Spring's Meteors on the Martian Atmosphere and Ionosphere

M. M. J. Crismani[1], N. M. Schneider[1], J. S. Evans[2], J. M. C. Plane[3], J. D. Carrillo-Sánchez[3], S. Jain[1], J. Deighan[1], and R. Yelle[4]

[1]Laboratory for Atmospheric and Space Physics, University of Colorado Boulder, Boulder, CO, USA, [2]Computational Physics, Inc., Springfield, VA, USA, [3]School of Chemistry, University of Leeds, Leeds, UK, [4]Lunar and Planetary Laboratory, University of Arizona, Tucson, AZ, USA

Key Points:
- Comet Siding Spring's meteor shower allows for the only remote sensing observations of Mg, Fe^+, and Fe in the Martian atmosphere
- We constrain the duration of the meteor shower to less than 3 hr, and the total meteoric fluence to 82,000 kg
- The distribution of these metallic ions defy expectation, prompting further study with 3-D global circulations models

Correspondence to:
M. M. J. Crismani,
matteo.crismani@colorado.edu

Citation:
Crismani, M. M. J., Schneider, N. M., Evans, J. S., Plane, J. M. C., Carrillo-Sánchez, J. D., Jain, S., et al. (2018). The impact of comet Siding Spring's meteors on the Martian atmosphere and ionosphere. *Journal of Geophysical Research: Planets*, *123*, 2613–2627. https://doi.org/10.1029/2018JE005750

Received 5 JUL 2018
Accepted 22 AUG 2018
Accepted article online 13 SEP 2018
Published online 17 OCT 2018

Abstract On 19 October 2014, comet C/2013 A1 (Siding Spring) had a close encounter with Mars and deposited cometary dust particles into the Martian atmosphere. We report a comprehensive analysis of the resulting meteor shower and its perturbation on Mars' atmosphere and ionosphere. Using Mars Atmosphere and Volatile EvolutioN/Imaging Ultraviolet Spectrograph observations of ablated meteoric metallic species, we show this shower lasted less than 3 hr and was therefore limited to one hemisphere. Meteoric ablation occurred in a narrow altitude layer, with Mg^+, Mg, Fe^+, and Fe deposited between about 105 and 120 km, consistent with comet Siding Spring's relative velocity of 56 km/s. We find that 82 ± 25 t of dust was deposited, improving previous measurements and a thousand times larger than model expectations. With regular observations over two Mars days, we show that horizontal winds globally redistribute this material and also suggest new vertical transport mechanisms for metallic ions. Such transport is inconsistent with diffusion and may be related to electrodynamic processes. The rapid loss of neutral species and presence of ions at high altitudes indicate that our understanding of existing Martian meteoric chemistry modeling and ionospheric dynamics is incomplete.

Plain Language Summary A close encounter of Mars with Comet Siding Spring resulted in the largest meteor shower in modern history, depositing orders of magnitudes more dust than a typical meteor shower. This unique event creates the opportunity to observe metallic species not normally observed, and their resulting chemistry and dynamics. This work constrains the duration of the meteor shower and revises the deposited cometary dust mass to 82,000 kg, more than the initial study and in excess of model expectations.

1. Introduction

On 19 October 2014, the dynamically new Oort cloud comet C/2013 A1 (Siding Spring) had a close encounter with Mars, passing within 141,000 km of the planet (McNaught et al., 2013). On a retrograde hyperbolic orbit, the comet made its closest approach to Mars at 18:29 UTC with a relative velocity of 56 km/s. In addition to gaseous deposition (Crismani et al., 2015), ionospheric perturbation (Gurnett et al., 2015; Restano et al., 2015), and magnetospheric interactions (Espley et al., 2015), comet Siding Spring also deposited cometary dust (Benna et al., 2015; Schneider et al., 2015) producing the only meteor shower detected at another planet.

Ablation occurs as interplanetary dust particles collide with ambient atmospheric gases at orbital velocities, leading to melting, vaporization, and the release of metallic atoms (e.g., Mg, Fe, and Na) in the upper atmosphere (Plane, 1991). Ablation typically occurs at an altitude where the pressure is ~1 μbar (Plane, Flynn, et al., 2018), corresponding to an average entry velocity of 11 km/s at Mars (Carrillo-Sánchez et al., 2016). Terrestrial metallic species have been well studied, and a model of ablation has been validated for the Earth (Vondrak et al., 2008). This understanding can be applied to comet Siding Spring's Martian meteor shower, accounting for the increased relative velocity (56 km/s) and relevant CO_2 dominant atmospheric chemistry (Plane, Carrillo-Sanchez, et al., 2018).

Meteor showers are common at the Earth; however, no significant enhancements in the terrestrial meteoric ion flux have been attributed to them (Grebowsky et al., 1998). While visible meteors are enhanced during meteor showers, visible meteors are composed of particles of mass 10^{-3} to 10^4 g and contribute a minor mass fraction (Flynn, 2002). In contrast, the primary mass contribution to the terrestrial metallic ion and neutral atom layers are sourced from ablated particles with masses less than 10^{-3} g.

Comet Siding Spring's meteor shower was exceptional due to its high fluence, originally constrained to between 2.7 and 16 t in less than a day (Schneider et al., 2015), compared to the *persistent layer* from sporadically ablating meteors (2–3 t/day; Crismani et al., 2017). For this reason, we observed more than 2 orders of magnitude enhancement to the metallic ion layer and were able to observe species (Mg, Fe^+, and Fe) not typically observable in the persistent layer (Mg^+). Although transient ionospheric layers observed in the Martian atmosphere have previously been attributed to meteor showers (Pätzold et al., 2005; Withers et al., 2008), Crismani et al. (2017) show these are unlikely to be formed from meteoric ablation.

Comet Siding Spring's meteor shower dust predictions ranged from meteor storm, depositing 10^7 kg, (Vaubaillon et al., 2014) to virtually nonexistent, with estimates below 100 kg (Kelley et al., 2014), where observations reported by Schneider et al. (2015) were closer to the *storm* end of this spectrum. Imaging Ultraviolet Spectrograph (IUVS) observations can resolve some characteristics of the cometary debris stream from observations of the aftermath of the meteor shower. Predictions suggested that dust ejected from the comet would remain confined in a debris stream that lagged behind the comet in its orbit and intercept the planet ~2 hr after closest approach (Tricarico et al., 2014). The dust was expected to impact the hemisphere near the morning terminator with a shower radiant close to the equator. Maximum dust deposition was predicted to occur between 19 October 19:59 and 20:09, and to last between 20 and 100 min.

2. Observations, Data Processing, and Model Details

2.1. Observing Geometry

The Mars Atmosphere and Volatile EvolutioN (MAVEN) mission entered an elliptical orbit around Mars on 21 September 2014, about a month before the comet encounter, with a primary mission intended to study the upper atmosphere and the escape of its constituent gases to space (Jakosky, Lin, et al., 2015). While designed to study the response of Mars' upper atmosphere to solar influences (Jakosky, Grebowsky, et al., 2015), it was fortuitously well instrumented to observe this unique cometary interaction.

MAVEN's remote sensing instrument for investigating the upper atmosphere is the IUVS (McClintock et al., 2015). This instrument's separate channels observe in the far and middle UV (110–190 and 190–340 nm). IUVS measures atmospheric emissions from CO_2, its dissociation, and ionization products, atomic and molecular species such as O and N_2, as well as meteoric ions and neutrals. During MAVEN's periapse observing mode, the IUVS instrument uses a scan mirror to construct vertical profiles of emergent radiation from the atmosphere at the limb, over the altitude range 90–250 km. Each orbit, IUVS takes up to 12 limb scans in a ~22-min observation period spanning ~45° around the planet.

The periapse segment of the MAVEN orbit was designed to provide geographic coverage with similar observing conditions within about five orbits. For example, the geographical (latitude and longitude) footprint of the spacecraft every fifth orbit, such as orbits 109 and 114, are, for our purposes, not significantly different. Periapse scans for the Siding Spring encounter begin at high latitudes and move toward the equator, from latitudes of 50°N to 5°S and from local times of 10 to 14 hr as the scans move from west to east geographic longitudes. We distinguish scans taken in the beginning or end of periapse as western or eastern, respectively.

To minimize potential risk to the spacecraft, MAVEN's orbit was phased to place the spacecraft behind Mars (relative to the dust flux) at the predicted time of maximum dust deposition. During this time, the spacecraft was commanded into a protective mode and IUVS halted observations. The Siding Spring encounter is composed of observations that were taken from orbit 109 (18 October 16:05 UT) to orbit 128 (22 October 07:49 UT), with the exception of orbit 115, when IUVS temporarily halted observations.

2.2. Spectral Emissions and Vertical Profiles

In Figure 1 we use IUVS observations of the Mars atmosphere taken after the comet's closest approach to identify two multiplets originating from Fe II and Fe I, the Mg I line, and the previously observed Mg II doublet. The Mg II doublet at 280 nm was present in pre-encounter observations and for the remainder of the mission as a persistent layer attributable to the ablation of sporadic meteors (Crismani et al., 2017). MAVEN's Neutral Gas and Ion Mass Spectrometer (NGIMS) instrument (Benna et al., 2015) also detected Mg^+ and Fe^+ during the Siding Spring encounter, as well as 10 other ions. We report no detection of the other NGIMS ions during

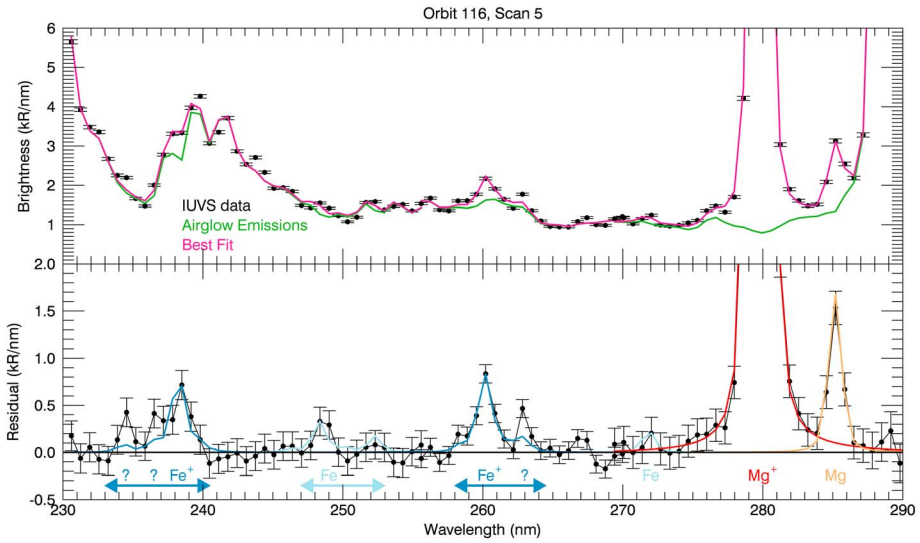

Figure 1. (top) Imaging Ultraviolet Spectrograph (IUVS) spectrum (black) taken after the close approach of comet Siding Spring, compared to two model spectra: (green) ambient atmospheric species (CO, CO_2^+, N_2, etc.) with scattered solar continuum from the Martian surface and (pink) the addition of ablated metallic species emissions (Mg II, Mg I, Fe II, and Fe I). These data are the result of a 4.4-s integration co-added over the 10° slit at 115-km altitude. Error bars represent one standard deviation and are constructed from the Poisson noise of the detector. (bottom) The difference between the IUVS data (black, top) and the ambient species emission (green, top) gives the residual emission (black, bottom), which is used to retrieve metallic species densities.

this period; however, the expected brightnesses of emission from these ions (apart from Mg^+ or Fe^+) would have been below IUVS' sensitivity or out of its wavelength range and therefore this result is not unexpected.

All metal emissions discussed herein are due to resonant scattering of solar UV photons, rather than direct excitation during ablation. The model spectrum for each species was constructed using their respective line positions, atomic constants for resonant scattering, and the solar Mid-UV spectrum (A'Hearn et al., 1983; Dymond et al., 2003; Kelleher & Podobedova, 2008; McClintock, 2014; Smith et al., 1995). Metallic species emission brightnesses were extracted from a composite spectrum fit of emission from ambient atmospheric gases through multiple linear regression fits of independent spectral components, and subsequently co-added by altitude (Stevens et al., 2011). Data processing techniques are outlined in detail in previous MAVEN/IUVS papers (Crismani et al., 2017; Evans et al., 2015; Jain et al., 2015; Schneider et al., 2015; Stevens et al., 2015).

Residual brightness (indicated by *?* in Figure 1) is found in high signal-to-noise ratio spectra from orbits 116–118 that suggest an unresolved issue when comparing observations to expected metal multiplet shapes. This excess brightness appears to be correlated with the multiplet shape of Fe II at 238 and 260 nm, indicating that discrepancies may exist between measured and observed atomic constants (Kramida et al., 2015), or some other unknown reason. The local atmospheric temperature is determined from concurrent observations of CO_2; however, we were unable to construct a non-LTE spectral emission model that was consistent with observations (Jain et al., 2015). The excess brightness is seen in most scans and altitudes where Fe^+ emission can be observed, is strongest near 110 km, and does not correspond to any other expected metallic emission. The excess brightness does not greatly impact the analysis or resulting conclusions, as the bulk of this work focuses on Mg^+.

We infer abundances from IUVS measurements using the Generalized Retrieval and ANalysis Tool. This tool merges the Atmospheric Ultraviolet Radiance Integrated Code model (Evans et al., 2015; Strickland et al., 1999) with OPTimal estimation retrieval algorithms (Lumpe et al., 1997, 2002, 2007). Atmospheric Ultraviolet Radiance Integrated Code uses the REDISTER algorithm (Gladstone, 1982) to model optically thick emissions after initial deposition. The important atomic parameters for the transitions of interest in this study are provided in Table 1. These parameters include the following: the line center wavelength for the transition, the statistical weight of the ground state sublevel, f_{lu} (oscillator strength), A_{ul} (transition probability), x_0 and x_1 (dispersion and offset of double-Gaussian fit to solar line profile measured in Doppler units at an arbitrarily chosen reference temperature of 150 K, referred to as *standard Doppler units*; see Gladstone, 1988), the line center

Table 1
Atomic Parameters and Solar Fluxes Used in the Retrievals of the Meteoric Species Densities Reported Herein

Feature	Wavelength (A)	Statistical weight	f_{lu}	A_{ul} (10^7 s^{-1})	x_o (SDU)	x_l (SDU)	Scattering cross section (10^{-12} cm^{-2})	Voigt parameter (10^{-3})	πF (ph·cm^{-2}·s^{-1})
Fe^+ (4p z ^{6}D° 7/2 − 4 s a ^{6}D 9/2)	2586.64	8	0.0717	8.94	108.55	113.57	1.31	8.71	3.515E+11
4p z ^{6}D° 9/2 − 4 s a ^{6}D 9/2	2600.17	10	0.239	23.5	51.73	40.94	4.4	23.0	1.882E+11
Fe $3d^6(^5D)4s4p(1P°)$ y ^{5}P° 3 − $3d^64s^2$ a ^{5}D 4	2719.83	7	0.122	14.2	30.73	35.37	2.35	14.5	2.568E+11
Mg^+ $2p^63p$ ^{2}P° 3/2 − $2p^63s$ ^{2}S 1/2	2796.35	2	0.608	26.0	47.80	54.46	7.93	18.1	1.79E+12
$2p^63p$ ^{2}P° 1/2 − $2p^63s$ ^{2}S 1/2	2803.53	2	0.303	25.7	42.66	49.13	3.96	17.9	1.41E+12
Mg 3s3p ^{1}P° 1 − $2p^63s^2$ ^{1}S 0	2852.96	3	1.8	49.1	25.45	24.24	24.0	34.8	1.97E+11

Note. Kramida et al. (2015).

scattering cross section (also calculated at the model reference temperature of 150 K), the Voigt parameter (i.e., the ratio of natural line broadening to Doppler line broadening, also calculated at the model reference temperature of 150 K), and πF (total flux in a given line incident on the upper boundary of the atmosphere). Our forward model calculations assume that the atmosphere is spherically symmetric along the line of sight, which is a safe approximation at Mars for solar zenith angles relevant to the observations considered here. After orbit 119 densities have decreased such that they are optically thin at line center and can be retrieved using an Abel transform (Chamberlain & Hunten, 1990) assuming single scattering with no absorption. Retrieved forward model brightness profiles are calculated from metallic species densities obtained by modifying an a priori guess until an optimal solution is found. We use 1-D model predictions (section 2.3) as a priori density values for the retrievals. Uncertainties in retrieved densities reported herein are determined through strictly formal error propagation of IUVS random uncertainties and estimated uncertainties in the a priori densities. Systematic uncertainties in retrieved densities (not reported) are a combination of uncertainties in the parameters in Table 1 and the IUVS MUV calibration uncertainties, estimated to be ±30%.

Careful attention has been paid to determine whether variations in the vertical profiles or horizontal distributions of emissions are the result of random or systematic errors. We use the strong correlation in brightness between adjacent slit elements and from scan to scan to conclude that random noise cannot produce spectral emissions or profiles. For example, Figure 4, right, shows that vertical profiles of retrieved Mg^+ and Mg densities in orbit 116 are detected consistently at similar altitudes and in similar abundances from scan to scan. We have also compared these profiles to other retrieved emissions, such as the CO_2^+ Ultraviolet Doublet and the reflected solar continuum, which are produced by photodissociation and reflection from dust in the lower atmosphere, respectively. That these emissions demonstrate differing vertical profiles indicates a different production process and suggests that these emissions represent detections and are not the result of a systematic error in data processing.

The results of Schneider et al. (2015) used the preliminary radiometric calibration available at the time. This work uses the updated calibration made possible by more extensive stellar calibration and cross calibration with the Mars Express SPICAM instrument (Leblanc et al., 2006). The revised calibration places observed brightnesses near the high end of the range reported previously and significantly reduces the density systematic uncertainty that was ascribed therein from ±300% to ±30%.

2.3. Atmospheric Modeling

A 1-D model of the Martian atmosphere (30–200 km, 0.5-km resolution) was used for this study. The vertical profiles of atmospheric composition (CO_2, O, O_2, H_2O, H, O_3, O_2^+, and electrons), temperature, and eddy

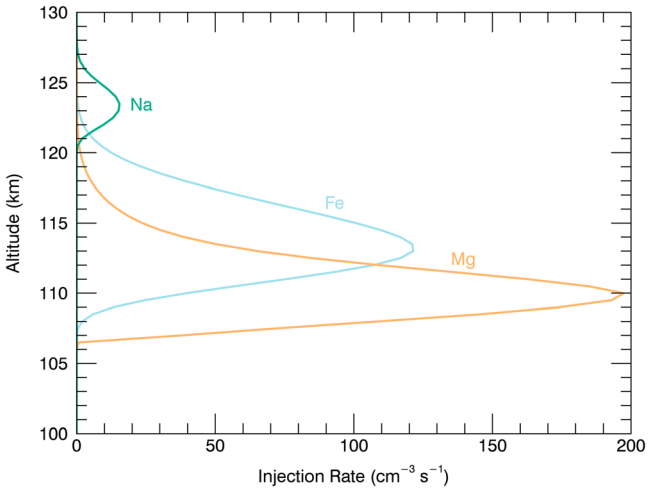

Figure 2. Modeled injection rates of Mg, Fe, and Na (atom·cm^{-3}·s^{-1}) as a function of altitude for comet Siding Spring dust entering Mars atmosphere at 56 km/s. The cometary dust size distribution is taken from Moorhead et al. (2014), with an assumed density of 2000 kg/m^3 and a chondritic composition. The injection of Mg at altitudes below Fe, despite the former's expected volatility, is due to Mg existing in a very stable oxide in the molten particle (Bones et al., 2018).

diffusion coefficient are described in detail elsewhere (Plane, Carrillo-Sanchez, et al., 2018). The injection rates from meteoric ablation of Mg/Mg$^+$ and Fe/Fe$^+$ as a function of altitude are determined using the Chemical ABlation MODel (Plane, Carrillo-Sanchez, et al., 2018; Vondrak et al., 2008; Figure 2). The Mg chemistry in the 1-D model was optimized to agree with the IUVS-measured peak of the persistent layer of Mg$^+$ near 95 km, which is produced by sporadic meteors (Crismani et al., 2017; Plane, Carrillo-Sanchez, et al., 2018). The Fe chemistry is taken from Whalley and Plane (2010) and is based on a significant database of measured rate coefficients for both neutral and ion-molecule reactions (Plane et al., 2015). Because the persistent (i.e., global background) Fe$^+$/Fe layers in the Martian atmosphere have not been retrieved by IUVS, this chemistry has not been optimized, in contrast to the Mg$^+$ chemistry.

The model is run for local noon equatorial conditions and does not include any magnetic or electric field effects, which should contribute to the vertical transport of the ions and hence influence their scale heights (section 3.4), particularly in regions with strong remnant crustal magnetism. However, for simplicity these effects are not considered here. The molecular diffusion coefficient is specified for a homopause region near 120 km, consistent with measurements made by the NGIMS instrument on MAVEN (Bougher, Jakosky, et al., 2015). The ablation profile should shift with altitude as a function of mesospheric temperature, with lower temperatures lowering the ablation height (Jakosky et al., 2017). This is taken into account when comparing retrieved densities to the model, and we find the retrieved ablation peak is ~2 km higher than the modeled peak altitude, which is within the uncertainty in the IUVS vertical attitude sampling.

For modeling the perturbation caused by Siding Spring, Chemical ABlation MODel was used to determine the injection of metal atoms ablating during a period of 4,800 s while the planet passed through the comet's coma (Schneider et al., 2015). The model's cometary dust size distribution is that of Moorhead et al. (2014). The model is then run for more than 60 hr with relevant vertical transport and chemistry (Figure 3). Because the Siding Spring dust entered the atmosphere at a velocity of 56 km/s, the peak ablation altitudes are ~30 km higher than predicted for the persistent layer (Crismani et al., 2017; Plane, Carrillo-Sanchez, et al., 2018). The correlation of dust velocity with ablation altitude is counterintuitive when compared to auroral or energetic particle processes. However, the ablation process raises the particle's temperature to its melting point, and a threshold amount of momentum needs to be transferred in collisions with ambient gases. Therefore, if the particle is traveling faster, fewer collisions are needed to affect the same increase in temperature, hence the higher altitude of ablation. In addition, the particle will have less time to radiatively cool.

The total mass injections into the planetary hemisphere facing toward the comet are 11.9, 5.9, and 0.3 t, for Mg, Fe, and Na, respectively, corresponding to a total cometary dust input of about 82 t in one hemisphere of Mars. These ratios of the mass input function are set by particle composition and size, and scaled to be consistent with the Mg$^+$ concentrations of orbit 116. One effect of the relatively high entry velocity of the Siding Spring dust is that a significant fraction of the evaporating metal atoms would have ionized immediately through hyperthermal collisions with CO_2 molecules. Using the ionization efficiencies recently reported by Janches et al. (2017), ~60% of the Mg atoms, 60% of the Fe, and 90% of the Na would have ionized. This is in contrast to the persistent layer, which is mostly ionized through charge exchange with O_2^+ (Molina-Cuberos et al., 2003).

3. Analysis and Interpretation

3.1. Hemispheric Dust Deposition

The spatial distribution and orbit-by-orbit evolution of Mg$^+$ reveal that ablation occurred only on one hemisphere (hereafter called the exposed hemisphere, Figure 4). IUVS periapse observations are separated by MAVEN's 4.5-hr orbital period, which we use as a reference timescale in the discussion below. The tangent points of limb scan observations on orbits 116 and 117 were on the exposed hemisphere during the time of

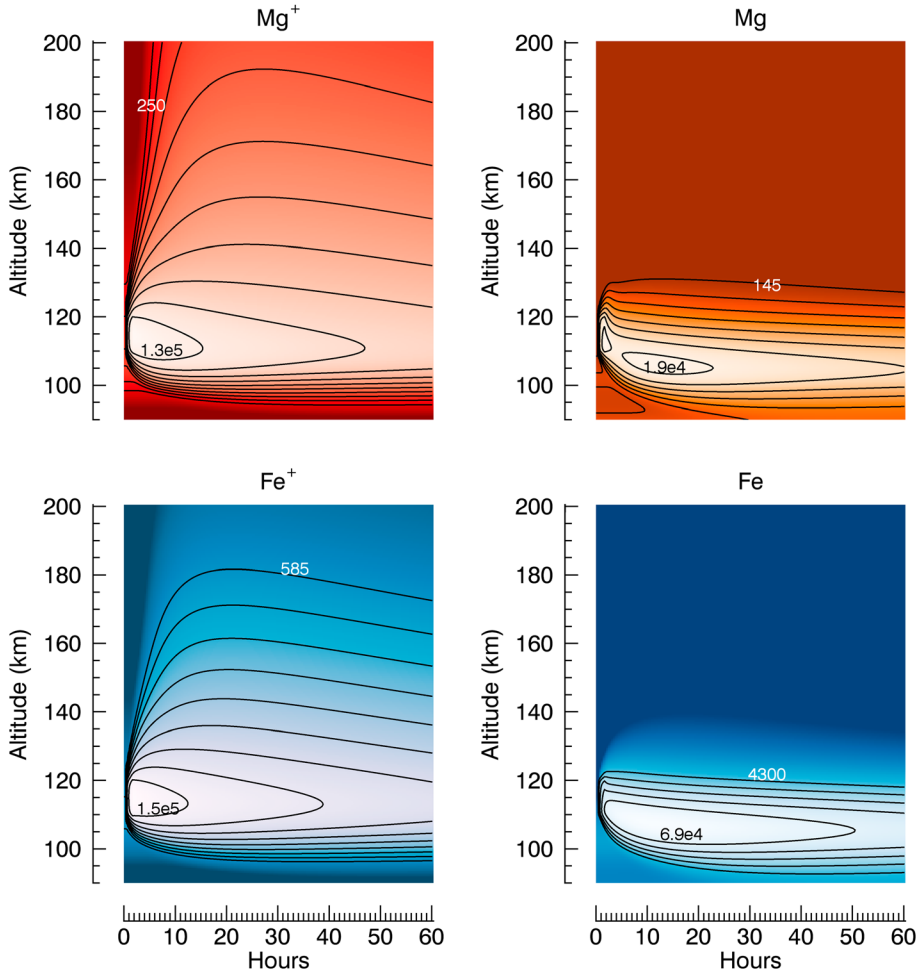

Figure 3. Modeled distributions of Mg^+, Mg, Fe^+, and Fe as a function of height and time following the injection of Siding Spring dust into the Martian atmosphere, starting at $t = 1$ hr. Contours represent changes in density by a factor of 2, with Imaging Ultraviolet Spectrograph detection limit (cm^{-3}) for each species (white) and values in the largest contour (black).

predicted deposition, with the geographic footprint of orbit 116 in the morning quadrant and orbit 117 in the predawn quadrant. By comparing the geographic distribution of Mg^+ between orbits 114, 116, and 117, and then to variations within orbit 116, we can progressively reduce the possible encounter time to 3.5 hr, constraining the deposition to a single hemisphere.

Consideration of the overall Mg^+ abundance and its vertical distribution offer increasingly tighter constraints on the duration of the meteor shower. We can constrain the timescale for the onset of deposition to less than 9 hr, as metallic emissions observed in orbit 114 are indistinguishable from background conditions. If IUVS had made observations during orbit 115, the predicted time of maximum dust deposition, we would not have expected these observations to contain significant Mg^+, as the observed region was on the dayside edge of the exposed hemisphere (Figure 4, left). We infer that the region observed during orbit 118 must not have been exposed to significant deposition, as the total vertically integrated Mg^+ content is less than 20% of that found in orbits 116 or 117. Furthermore, the layer of Mg^+ from orbit 118 lies above altitudes where deposition can occur (section 3.3) and must have been transported there.

The tightest constraints on timescale come from a comparison of relevant deposition timescales and total Mg^+ abundances observed in orbits 116 and 117. Deposition is expected to be spatially uniform as Mars is small (~7000 km) compared to the scales appropriate for cometary debris streams (hundreds of thousands of kilometers). To first order, the cumulative amount of Mg^+ deposited at a geographic region is proportional to the time it spent on the exposed hemisphere during deposition. Therefore, if the duration of the shower is

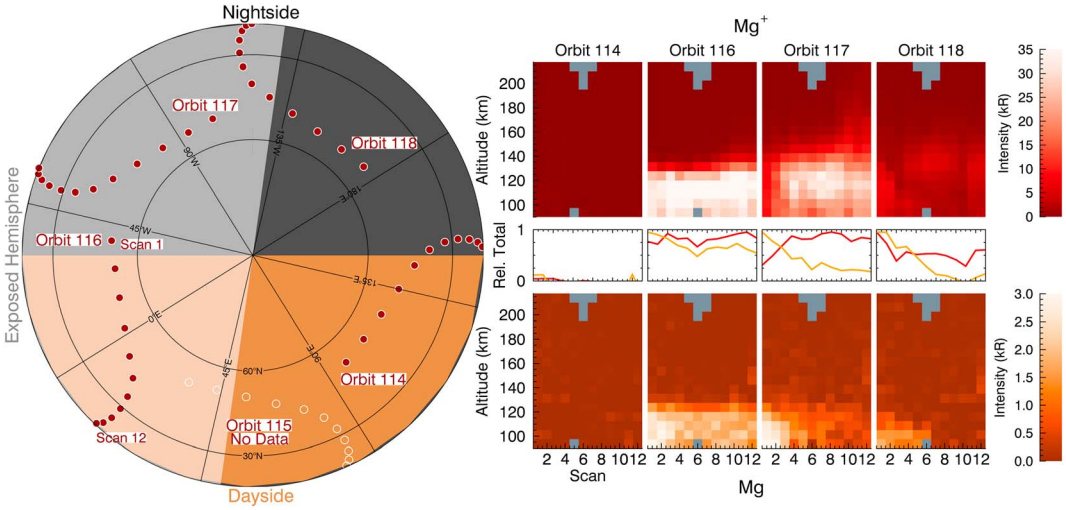

Figure 4. (left) A geographical representation of observed regions of Mars at the predicted time of dust deposition, where the tangent points of orbits 114, 116, 117, and 118 are shown with maroon circles. Scans begin at high latitudes and end near the equator, moving from west to east. The spacecraft stays fixed with respect to the sun (to the bottom of this image), and the planet rotates underneath it, creating Mars Atmosphere and Volatile EvolutioN's latitude coverage. (right) Orbit by orbit images of emission from Mg^+ and Mg (top and bottom) constructed with tangent altitude shown on the vertical axis, and adjacent scans are shown on the horizontal axis, which span 1,000 km across the planet. Mg^+ emission brightnesses in orbit 116 exceed 35 kR and are intentionally saturated to highlight medium and dim features. Line plots (Mg^+ = red, Mg = orange) in the center of the images indicate the mean vertical brightness between 90 and 180 km, normalized to each orbit. Observations before the comet's passage (orbit 114) are consistent with the persistent layer of Mg^+ and no observable Mg in the atmosphere.

long compared to 4.5 hr (MAVEN's orbital period), the geographical locations observed in orbit 117 would have experienced greater deposition and would have had significantly more Mg^+. In fact, we see the opposite, where Mg^+ in orbit 117 is ~80% of that in orbit 116, indicative that the timescale for deposition was shorter than MAVEN's orbital period (<4.5 hr).

We further constrain the deposition timescale by considering the abundance of Mg^+ in orbit 116 from west to east scans. If deposition lasted as much as 4.5 hr, western scans would remain in the exposed hemisphere for the entire deposition period, whereas eastern scans would become shielded in 3 hr. Therefore, western scans would be expected to have 1.5 times more Mg^+ than eastern scans. In fact, the ratio of the Mg^+ vertical abundance of the four most western scans to the four most eastern scans is 0.9, indicative that the most intense deposition could have lasted no longer than ~3 hr. This is consistent with the timescales of the 1-D model used here, which assumes deposition occurs over ~1.5 hr (section 2.3).

3.2. Deposition and Initial Evolution

Cometary deposition provides a unique opportunity to observe the response of the Martian ionosphere to a significant perturbation. Emission from metallic ions and neutrals observed in orbit 116 peak in intensity around 110–120 km and decrease rapidly with increasing altitude (Figure 5, left). The ions have a roughly exponential emission scale height of ~5 km, compared to concurrent observations of the CO_2 atmosphere with an ~14 km scale height. The small scale height of the metallic ions implies that these species are not yet well mixed and suggests that deposition occurred in a narrow layer only 10–20 km thick with a peak altitude near 115 km, consistent with ablation speeds of 56 km/s. Comparing Mg^+ in orbit 116 to the model, we find this interpretation is consistent with model predictions (Figure 6). Ionograms obtained by the Mars Express MARSIS experiment observed a transient enhancement during this time period (Gurnett et al., 2015), and recent updates to their data processing suggest that the altitude of this layer is consistent with our observations (A. Kopf, personal communication, August 14, 2018, University of Iowa). Dynamical transport and chemical reprocessing become entwined after initial deposition, as demonstrated when comparing orbits 116 and 117 (4.5 and 9 hr after deposition, respectively).

Persistent layer observations of Mg^+ (Crismani et al., 2017) offer the only constraints on the meteoric chemistry of atomic Mg, which can be, but has not been, observed by IUVS. Figure 6 demonstrates that the chemical model from Plane, Carrillo-Sanchez, et al. (2018) does predict the abundance of Mg to a

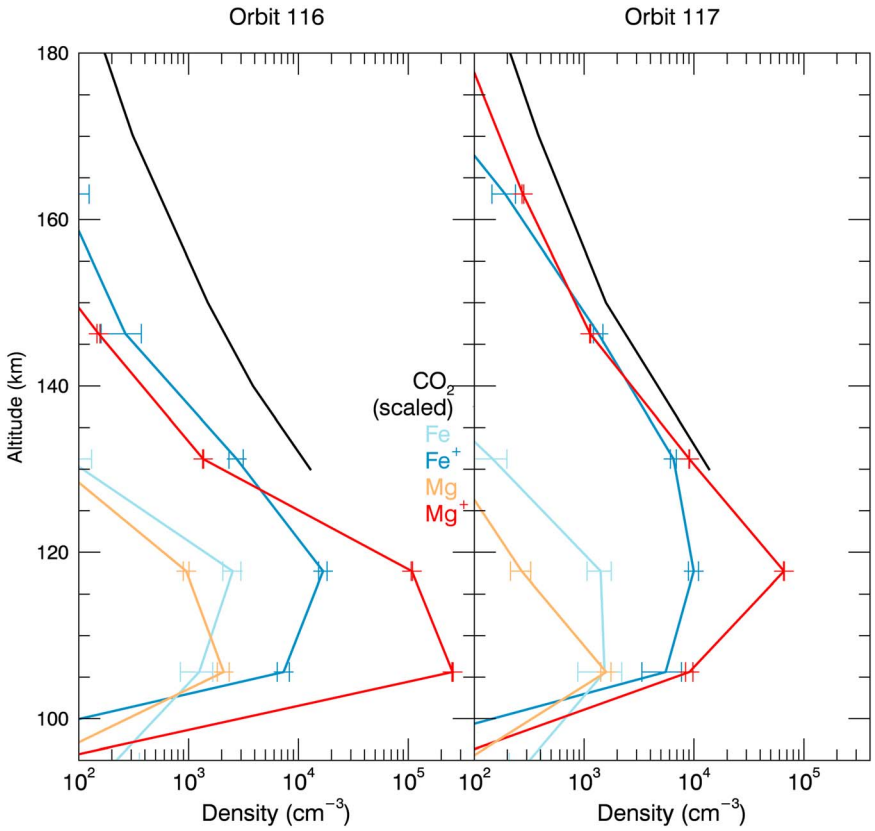

Figure 5. Profiles of neutral and ionized metallic species densities (cm^{-3}) from orbits 116 (left) and 117 (right), averaged across each orbit, where the uncertainties are given by standard error propagation of the retrievals. These metallic species are compared to the neutral CO_2 density from concurrent Imaging Ultraviolet Spectrograph observations, for which retrievals are constrained to altitudes above 130 km (approximate peak of emission). It should be noted that scan-to-scan variations in metallic species do exist and are addressed below in Figure 8.

reasonable accuracy. However, as these are the only observations of Fe^+ and Fe in the atmosphere of Mars, it is not surprising that, though the shape of Fe^+ and Fe are roughly consistent, the model overestimates their abundances. This may be due to chemical sinks that have not yet been considered by the model, or due to horizontal or vertical transport.

Comparing subsequent orbits from the exposed hemisphere provides temporal insight in the evolution of this meteoric perturbation. The region observed in orbit 117 (Figure 5, right panel) differs from the geographical location in orbit 116 (left panel); however, these both represent the exposed hemisphere and deposition is not expected to vary on these spatial scales. In both orbits, neutral emissions show scale heights of ~5 km and do not extend into the upper atmosphere, which, unlike the ions, we interpret as suppression of the neutrals by rapid charge exchange with O_2^+.

The spatial distribution of neutral Mg in a single orbit after deposition provides constraints to its lifetime against ionization and incorporation in meteoric molecules. Western scans differ from eastern scans in their dayside exposure, where eastern scans spend close to 4 hr longer in sunlight. In orbit 116, there is a 50% reduction of Mg abundance from western to eastern scans, and in orbit 117 this reduction is closer to 75% (Figure 4, right bottom row). This rapid loss of neutral Mg is not fully captured by the 1-D model (sections 2.3 and 3.5), despite the new chemistry that was developed to account for the lack of observable Mg in the persistent layer (Crismani et al., 2017; Plane, Carrillo-Sanchez, et al., 2018). The 1-D model's absence of horizontal winds and diurnal variation may suggest the mechanisms for this rapid loss of the neutral species.

3.3. Rapid Horizontal and Vertical Transport of Metallic Species

The hemispheric injection of metals provides insight into the global motions of the atmosphere. Figure 7 shows the spatial distribution and temporal evolution of Mg^+ abundance over four sequential orbits. Both

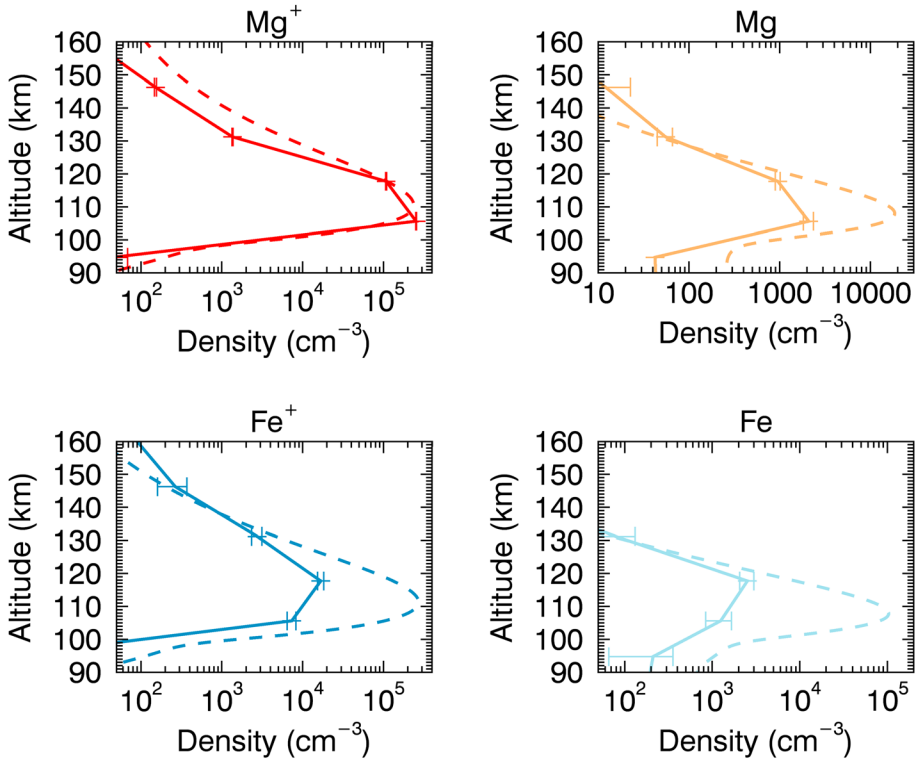

Figure 6. Vertical profiles of retrieved metallic species densities from Imaging Ultraviolet Spectrograph observations during orbit 116 (as in Figure 3) compared to the 1-D model (dashed). These retrieved densities are averaged across the orbit; therefore, they do not represent spatial and vertical variability that exists for each of the species (see Figure 4). The model profiles are scaled to the retrieved densities of Mg+, whose chemistry is most closely constrained by previous Imaging Ultraviolet Spectrograph observations (Plane, Carrillo-Sanchez, et al., 2018).

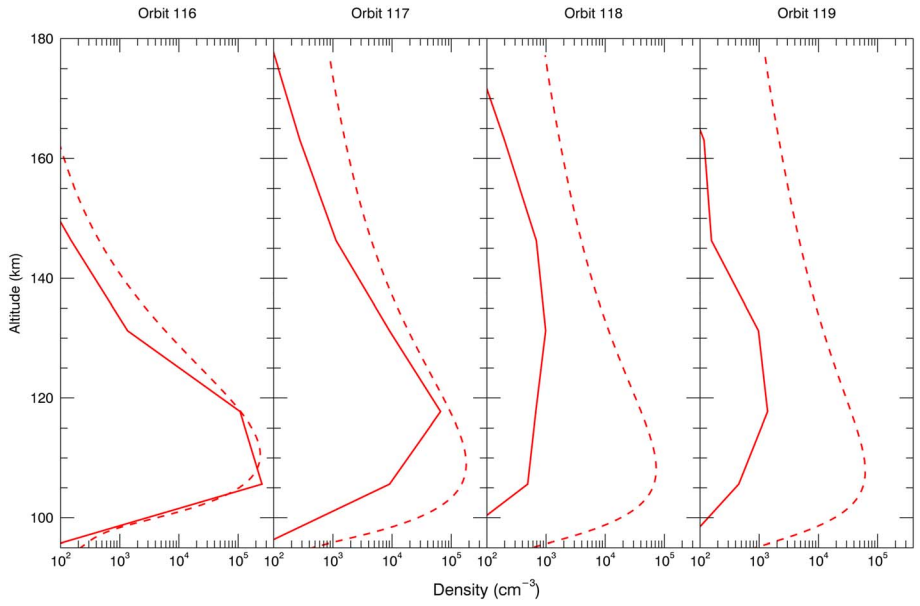

Figure 7. Altitude profiles of Mg^+ densities retrieved from Imaging Ultraviolet Spectrograph observations (solid) compared to a 1-D atmospheric model (dashed), averaged over the middle of the periapse segment (scans 4–7) to avoid scan-dependent variability (discussed in Figure 8). The tangent points of each of these orbits can be found in Figure 4, where orbit 114 and orbit 119 have roughly the same geographical locations. Deposition occurs at an altitude consistent with an entry velocity of 56 km/s, and with good agreement in orbit 116. Since this velocity is close to the dynamical limit for a body interacting with Mars, deposition of Mg^+ cannot occur higher than the observed 110–120 km.

Mg^+ and Fe^+ are readily observed in all scans of orbits 116–124 (more than 40 hr after closest approach) and their abundances on the unexposed hemisphere implies global redistribution.

The presence of metallic species in orbit 119, antipodal to the meteor shower radiant at the time of predicted dust deposition, constrains the horizontal wind speed to within 180–240 m/s. We determine these values by assuming that the region of orbit 117 is the source of ions observed in orbit 119 and that this material has been transported across the nightside. The upper value assumes that deposition occurred over a 3-hr period. However, if the deposition timescale were shorter (~100 min expected from Moorhead et al., 2014) the lower wind speed may be more appropriate. These values are consistent with model expectations, which predict speeds of 160–260 m/s at altitudes of 100–120 km (Bougher et al., 1999; Bougher, Pawlowski, et al., 2015).

The presence of metallic ions in orbit 118 above deposition altitudes (Figure 7) indicates that they must have been vertically transported, and by means that are not yet understood (section 3.4). Orbits 117 and 118 demonstrate vertical transport that exceeds reasonable effective diffusion velocities (1 m/s) as determined from our 1-D model and may indicate bulk vertical motion. More perplexing is the similarity in spatial distribution between orbits 119 and 116, despite their geographic footprints occurring on opposite sides of Mars. If vertical transport produces the flow of ions in orbit 117 and 118, they do not appear to affect those in orbit 119 for unknown reasons.

Mass separation above the homopause (~120 km) would be expected for Fe^+, Mg^+, and CO_2, as these species are in a region of the atmosphere where the mean free path of particles is large enough that molecular diffusion dominates, and the vertical diffusion of the ions should be ambipolar. Therefore, the scale heights of Mg^+ and Fe^+ should be double those of their neutral species such that $H_{CO2} < H_{Fe} < H_{Mg}$ (Rees, 1989). However, both metallic species exhibit a scan-averaged common scale height comparable to CO_2 (Figure 5). While CO_2 density profiles do not strongly depend on latitude or solar zenith angle, metal ion profiles vary from scan to scan. Western scans in orbit 117 have a scale height of ~8 km, more shallow than the neutral atmosphere with a scale height of ~14 km, while eastern scans appear to have a comparable exponential decay (Figure 8). It is not clear what is causing this variation, as it is not seen in any ambient ions or neutrals, and not expected from standard atmospheric dynamics.

Lack of mass separation in metal ions has also been observed in situ by NGIMS above the homopause (Grebowsky et al., 2017), though that study did not report a uniform profile with a slope that exceeds the neutral atmosphere as expected from ambipolar diffusion. Ambient ions such as CO_2^+ and O_2^+ are strongly regulated by the neutral atmosphere and dissociative recombination electrons, and so have lifetimes on the order of minutes, whereas metallic ions can have recombination lifetimes in excess of hours or even days (Whalley & Plane, 2010). Therefore, metallic ions are the only species to demonstrate this behavior, as ambient ions reflect their production and chemical conditions, not large-scale ionospheric transport.

3.4. Potential Mechanisms for Anomalous Vertical Transport

There are two plausible electrodynamic mechanisms that could create the anomalous ion scale heights seen in Figure 5: a Lorentz force that acts as a magnetic *diffusivity*, or an ambipolar electric field. There can be strong vertical magnetic field gradients in the altitude range 100 to 200 km, depending on the solar ionizing flux at these altitudes (Brain et al., 2005). It is possible that these gradients and misalignment of the field with horizontal winds may lead to Lorenz forces acting on the metallic species. This mechanism cannot be considered promising, however, until further modeling, which is beyond the scope of this work, determines whether these forces produce vertical drift comparable to the diffusion speeds of 1 m/s, and in any case would be limited to regions with residual magnetic fields.

Ambipolar electric fields at Mars have been shown to cause enhanced loss of O_2^+ (Ergun et al., 2016; Collinson et al., 2017; Lillis et al., 2018). These ions are drawn from below the exobase by the loss of electrons due to enhanced heating, creating an *E* field that drags ions out of the ionosphere, and have been similarly observed at Venus (Collinson et al., 2016). Typically, these ions are affected down to 160 km, so it is plausible that metallic species undergo mass separation below this, and then are mixed above. Our observations are spatially coarse, such that we cannot make a statement here about separate scale heights with altitude. While ambipolar electric fields shown by Ergun et al. (2016) should be strong enough to lift Mg^+, which is 75% as massive

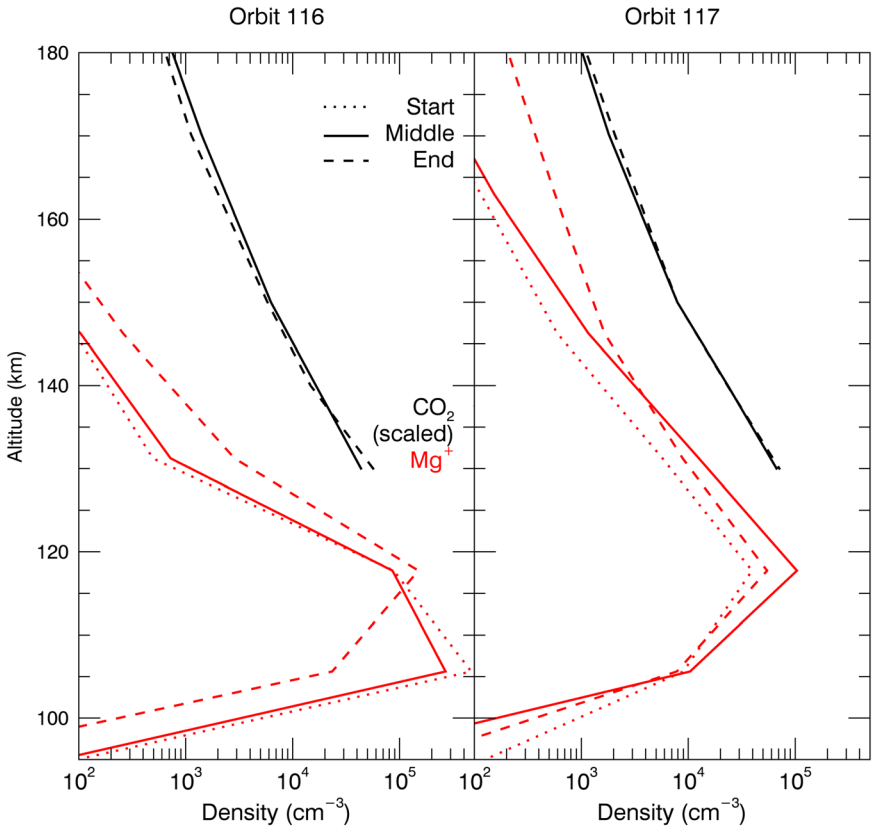

Figure 8. Altitude profiles of Mg^+ density (red) retrieved from Imaging Ultraviolet Spectrograph observations during orbits 116 (left) and 117 (right), averaged in sets of four scans (1–4, 5–8, and 9–12) and compared to the neutral CO_2 density (black). Scans are taken from west to east, with the former represented by the starting scans, and the latter represented by the end scans. These variations are not observed in the background CO_2 profiles obtained concurrently with these data.

as O_2^+, without appropriate modeling it is not immediately clear that ambipolar electric fields would be strong enough to affect Fe^+ with a mass that is 175% that of O_2^+.

3.5. Enhanced Loss of Metallic Species

Discrepancies between the observed total metallic abundance compared to those predicted by the 1-D model (section 2.3) highlight important physical and chemical processes that demand further investigation. We characterize the observed total metallic abundance for each species by summing densities between 90 and 180 km and across the periapse segment to give a general metric of the abundance of metallic species while smoothing the effects of horizontally or vertically disjoint profiles (section 3.6).

The 1-D model is run for quiescent Mars until steady state is reached, after which a meteoric perturbation is applied and we track the relaxation of the model for comparisons with observations. It is run for daytime low-latitude conditions and does not include diurnal variations. This model does not apply to the unexposed hemisphere, so we approximate horizontal transport by reducing the model after orbit 117 by a factor of 2 (equivalent to distributing the deposited material over the entire planet).

The total metallic abundance observed is less than predicted after orbit 117, indicating the rapid disappearance of metallic species compared to the current modeled processes. There may be a chemical process affecting both the Fe and Mg chemistry branches simultaneously; however, a dynamical loss process that affects all metallic species may be more likely. As ions deposited near 100–120 km diffuse vertically, if ions are being removed at the exobase at rates larger than predicted, this effectively depletes neutrals as well. The presence of ions at high altitudes in orbit 117 (Figure 5) suggests that this may be occurring. It would

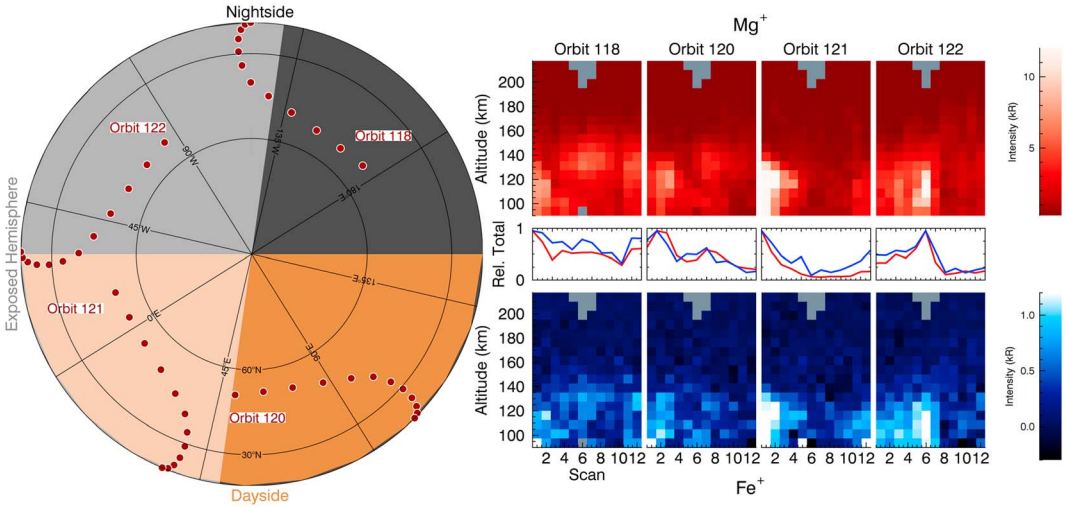

Figure 9. Examples of two unusual phenomena are shown here: Detached layers in orbits 118 and 120, and strong horizontal gradients in orbits 121 and 122. (left) As in Figure 4, a geographical representation of observed regions of Mars at the predicted time of dust deposition, where the tangent points of orbits 118, 120, 121, and 122 are shown with maroon circles, with scans beginning at high latitudes and ending near the equator, moving west to east. (right) Orbit by orbit images of emission from Mg^+ and Fe^+ (top and bottom, respectively) constructed with tangent altitude shown on the vertical axis, and adjacent scans shown on the horizontal axis, which span 1000 km across the planet. Line plots (Mg^+ = red, Fe^+ = blue) in the center of the images indicate the mean vertical brightness between 90 and 180 km, normalized to each orbit. Observations before the comet's passage (shown for Mg^+ in Figure 4) are consistent with the persistent layer of Mg^+ and no observable Fe^+ in the atmosphere.

be necessary to model these species and their appropriate chemistry in a 3-D self-consistent way that includes magnetic fields. There is no Mars global circulation model that includes meteoric chemistry; doing so here would be outside the scope of this work.

Ions transported by electrodynamic processes end in two populations dependent on their initial vertical motion. Ions moving downward will neutralize and undergo appropriate metallic chemistry that either re-ionizes them or removes them to a stable sink, likely to be metal carbonates (Plane, Carrillo-Sanchez, et al., 2018). Ions drifting upward stay ionized and have lifetimes that increase with increasing altitude and may therefore leave the atmosphere much more rapidly than predicted by diffusion alone. While these ions would not have sufficient kinetic energy to escape thermally, there may be a multistep process to accelerate them along open field lines into the magnetotail as seen at Earth and Saturn (Christon et al., 2015, 2017) or through one of several ion outflow mechanisms seen at Mars (Brain et al., 2015).

3.6. Detached Layers and Strong Gradients

Figure 6 shows coherent structures and gradients that require further study. Deposition is expected to occur uniformly on the exposed hemisphere, and diffusion and transport should be smoothing processes over these spatial scales. However, in orbits 118 and 120, we see Mg^+ forms a distinct layer in the middle scans that is not directly connected to the Mg^+ in the beginning of those scans. This feature appears to be evident in the Fe^+ as well, although clearer in orbit 118 than 120. These ion layers occur at altitudes that are higher than deposition permits, indicating that this transport must be coherent on a spatial scales over 1000 km horizontally.

As noted by Schneider et al. (2015), and visible in Figure 9, there is an increase in Fe^+, Mg^+, and Mg in orbits 121 and 122 compared to previous orbits. This is due to an unexplained set of strong enhancements in scans 1 and 6 from each orbit, respectively, and not the whole set of scans. Moreover, the total amount of Mg^+ does not change significantly between orbits 118 and 122, yet the bulk of the ions are contained in the first six scans of orbit 122. The horizontal gradient in Mg^+, changing by a factor of 7 within two scans of orbit 122 is not readily explained and requires a mechanism yet to be determined.

The geographic regions observed during these orbits are on the exposed hemisphere and may suggest a local phenomenon where metallic species are confined within a small geographic region in a manner inconsistent with expected diffusion or standard transport. Similar confinement has been suggested for transient

metallic layers above the ablation region (Grebowsky et al., 2017), although no mechanism has yet been described. Three-dimensional modeling may be necessary to determine whether these ions become trapped in circulation patterns, are influenced by remnant crustal magnetization, or some other effect.

3.7. Revisiting Meteor Shower Predictions

The vertical profiles of Mg, Fe^+, and Fe density complement the Mg^+ profiles of Schneider et al. (2015), and this analysis provides an opportunity to revise the estimate and reduce the uncertainty of their reported dust flux. Their work carried a range of reported Mg^+ densities that implied a dust deposition mass bracketed between 2.7 and 16 t. In addition to the updated calibration, revisiting their work indicated an inappropriately low scattering efficiency factor. The updated values (Table 1) yield a delivered dust mass inferred by the Mg^+ measurements of 82 ± 25 t. Assuming a clear sky for an observer at the surface of Mars, with similar assumptions to Schneider et al. (2015), we revise the expected zenithal hourly rate to 5×10^5 meteors per hour, or 160 meteors per second. The Martian rovers would not have been able to observe this event however, since Opportunity was already in daylight and Curiosity was on the shielded hemisphere. Very bright fireballs may have been visible in the daylight; however, these make a small fraction of the overall meteor shower and it is unclear whether these would have been detected. Similarly, orbiting spacecraft were intentionally attempting to hide from this event, and we are unaware of any images of the planet or atmosphere that were taken during comet Siding Spring's closest approach.

There is a significant discrepancy between the observed (Schneider et al., 2015) and predicted (Kelley et al., 2014) dust deposition that may be related to dust size. The modeled dust was in the size range 0.7–3.6 mm, which were ejected from the comet no more than 1.5 years before the encounter. However, the shape and altitude of the observed ablation suggest that most of the impacting particles were in the size range 1–100 μm. As radiation pressure rapidly sweeps away smaller particles, it is expected that the impacting grains were younger than the 1.5-year-old modeled grains and therefore would be more sensitive to cometary activity before the encounter. While the relationship between dust delivery and cometary activity is not necessarily linear, the modeled water production rate of 4×10^{27} H_2O per second (Kelley et al., 2014), is smaller than the observed 1.2×10^{28} H_2O per second (Crismani et al., 2015) by a factor of 3. Moreover, as observations were limited by the lack of multiple observation epochs (Siding Spring is a dynamically new Oort cloud comet), some cometary parameters (such as grain ejection velocity) may not be well constrained.

4. Summary

Observations of comet Siding Spring's meteor shower provide a unique opportunity to observe the response of the Martian atmosphere and ionosphere to a significant perturbation. This time period provides constraints on metallic species that would otherwise be undetectable with current instruments and may shed light on new dynamics or the chemistry that affects them.

Using the spatial distribution of Mg^+ abundance around the planet, we determine that Mars passed through the debris stream of comet Siding Spring in no more than 3 hr. Dust from comet Siding Spring was deposited in a narrow vertical layer, as seen in all metallic species emissions observed by IUVS. Horizontal winds then distributed this material globally within 9 hr, requiring horizontal winds speeds at 120–150 km in the range of 180–240 m/s. Neutral Mg appears to be rapidly destroyed or lost on the dayside, where it becomes reduced by 75% within 8 hr, which is faster than current model predictions, suggesting an incomplete understanding of the processes that affect it.

Vertical transport of metallic ions is implied by the observations of enhanced densities at high altitude, which is not completely unexplained by diffusive transport in a 1-D model. This transport is more rapid than diffusion, coherent over 1,000 km horizontally, and may be related to electrodynamic effects. The presence of several other unexpected phenomena provides a potential case study for 3-D modeling efforts to determine how these anomalous structures and features are formed, and whether the presence of crustal magnetic fields has any effect.

We use this work to revisit meteor shower dust predictions where there is significant discrepancy compared to observations. The shape and altitude of the ablated layer suggests that particles that impacted Mars were smaller than modeled, and therefore more sensitive to the water production rate before the encounter. The

relationship between cometary activity and delivered dust mass is not necessarily linear, and we can therefore begin to understand this self-consistently by noting the observed water production rate was three times larger than predictions.

Acknowledgments
M. C. thanks J. Grebowsky and M. Benna for their insight on metallic ions and Z. Girazian, R. Lillis, L. Andersson, and C. Fowler for helpful discussions about the ionosphere. NASA supports the MAVEN mission through the Mars Scout program. J. M. C. P. and J. D. C-S. were supported by the European Research Council (project 291332-CODITA). All data used herein are available on the Atmospheres node of the NASA Planetary Data System, under periapse level 1c files. The retrieved concentrations presented in this work, from the IUVS periapse data, are available on the MAVEN Science Data Center (SDC) website hosted at LASP https://lasp.colorado.edu/maven/sdc/public/pages/datasets/iuvs.html. The authors declare no competing financial interests.

References

A'Hearn, M., Ohlmacher, J., & Schleicher, D. (1983). *Technical report: TR AP83–044*. College Park, MD: University of Maryland.

Benna, M., Mahaffy, P. R., Grebowsky, J. M., Plane, J. M. C., Yelle, R. V., & Jakosky, B. M. (2015). Metallic ions in the upper atmosphere of Mars from the passage of comet C/2013 A1 (Siding Spring). *Geophysical Research Letters*, *42*, 4670–4675. https://doi.org/10.1002/2015GL064159

Bones, D., Gómez Martín, J. C., Carrillo Sánchez, J. D., Dobson, A. J., & Plane, J. M. C. (2018). Characterisation of the extra-terrestrial magnesium source in the atmosphere using a meteoric ablation simulator. *Geophysical Research Letters*, *45*, 7765–7771. https://doi.org/10.1029/2018GL077427

Bougher, S., Engel, S., Roble, R. G., & Foster, B. (1999). Comparative terrestrial planet thermospheres: 2. Solar cycle variation of global structure and winds at equinox. *Journal of Geophysical Research*, *104*(E7), 16,591–16,611.

Bougher, S., Pawlowski, D., Bell, J. M., Nelli, S., McDunn, T., Murphy, J. R., et al. (2015). Mars Global Ionosphere-Thermosphere Model (MGITM): Solar cycle, seasonal, and diurnal variations of the Mars upper atmosphere. *Journal of Geophysical Research: Planets*, *120*, 311–342. https://doi.org/10.1002/2014JE004715

Bougher, S., Jakosky, B., Halekas, J., Grebowsky, J., Luhmann, J., Mahaffy, P., et al. (2015). Early MAVEN Deep Dip campaign reveals thermosphere and ionosphere variability. *Science*, *350*(6261), aad0459.

Brain, D. A., Halekas, J. S., Lillis, R., Mitchell, D. L., Lin, R. P., & Crider, D. H. (2005). Variability of the altitude of the Martian sheath. *Geophysical Research Letters*, *32*, L18203. https://doi.org/10.1029/2005GL023126

Brain, D., McFadden, J. P., Halekas, J. S., Connerney, J. E. P., Bougher, S. W., Curry, S., et al. (2015). The spatial distribution of planetary ion fluxes near Mars observed by MAVEN. *Geophysical Research Letters*, *42*, 9142–9148. https://doi.org/10.1002/2015GL065293

Carrillo-Sánchez, J., Nesvorný, D., Pokorný, P., Janches, D., Plane, J. M. C., et al. (2016). Sources of cosmic dust in the Earth's atmosphere. *Geophysical Research Letters*, *43*, 11,979–11,986. https://doi.org/10.1002/2016GL071697

Chamberlain, J., & Hunten, D. (1990). *Theory of planetary atmospheres. An introduction to their physics and chemistry*. San Diego, CA: Academic Press.

Christon, S. P., Hamilton, D. C., Plane, J. M. C., Mitchell, D. G., DiFabio, R. D., & Krimigis, S. M. (2015). Discovery of suprathermal Fe+ in Saturn's magnetosphere. *Journal of Geophysical Research: Space Physics*, *120*, 2720–2738. https://doi.org/10.1002/2014JA020906

Christon, S. P., Hamilton, D. C., Plane, J. M. C., Mitchell, D. G., Grebowsky, J. M., Spjeldvik, W. N., & Nylund, S. R. (2017). Discovery of Suprathermal ionospheric origin Fe+ in and near Earth's magnetosphere. *Journal of Geophysical Research: Space Physics*, *122*, 11,175–11,200. https://doi.org/10.1002/2017JA024414

Collinson, G. A., Frahm, R. A., Glocer, A., Coates, A. J., Grebowsky, J. M., Barabash, S., et al. (2016). The electric wind of Venus: A global and persistent "polar wind"-like ambipolar electric field sufficient for the direct escape of heavy ionospheric ions. *Geophysical Research Letters*, *43*, 5926–5934. https://doi.org/10.1002/2016GL068327

Collinson, G., Mitchell, D., Xu, S., Glocer, A., Grebowsky, J., Hara, T., et al. (2017). Electric Mars: A large trans-terminator electric potential drop on closed magnetic field lines above Utopia Planitia. *Journal of Geophysical Research: Space Physics*, *122*, 2260–2271. https://doi.org/10.1002/2016JA023589

Crismani, M. M. J., Schneider, N. M., Deighan, J. I., Stewart, A. I. F., Combi, M., Chaffin, M. S., et al. (2015). Ultraviolet observations of the hydrogen coma of comet C/2013 A1 (Siding Spring) by MAVEN/IUVS. *Geophysical Research Letters*, *42*, 8803–8809. https://doi.org/10.1002/2015GL065290

Crismani, M. M. J., Schneider, N. M., Plane, J. M. C., Evans, J. S., Jain, S. K., Chaffin, M. S., et al. (2017). Detection of a persistent meteoric metal layer in the Martian atmosphere. *Nature Geoscience*, *10*(6), 401–404.

Dymond, K., Wolfram, K. D., Budzien, S. A., Nicholas, A. C., McCoy, R. P., & Thomas, R. J. (2003). Middle ultraviolet emission from ionized iron. *Geophysical Research Letters*, *30*(1), 1003. https://doi.org/10.1029/2002GL015060

Ergun, R. E., Andersson, L. A., Fowler, C. M., Woodson, A. K., Weber, T. D., Delory, G. T., et al. (2016). Enhanced O2+ loss at Mars due to an ambipolar electric field from electron heating. *Journal of Geophysical Research: Space Physics*, *121*, 4668–4678. https://doi.org/10.1002/2016JA022349/pdf

Espley, J., DiBraccio, G. A., Connerney, J. E. P., Brain, D., Gruesbeck, J., Soobiah, Y., et al. (2015). A comet engulfs Mars: MAVEN observations of comet Siding Spring's influence on the Martian magnetosphere. *Geophysical Research Letters*, *42*, 8810–8818. https://doi.org/10.1002/2015GL066300

Evans, J. S., Stevens, M. H., Lumpe, J. D., Schneider, N. M., Stewart, A. I. F., Deighan, J., et al. (2015). Retrieval of CO_2 and N_2 in the Martian thermosphere using dayglow observations by IUVS on MAVEN. *Geophysical Research Letters*, *42*, 9040–9049. https://doi.org/10.1002/2015GL065489

Flynn, G. J. (2002). Near-Earth environment. *Meteors in the Earth's Atmosphere: Meteoroids and Cosmic Dust and Their Interactions with the Earth's Upper Atmosphere*, *77*.

Gladstone, G. (1982). Radiative transfer with partial frequency redistribution in inhomogeneous atmospheres: Application to the Jovian aurora. *Journal of Quantitative Spectroscopy & Radiative Transfer*, *27*(5), 545–556. https://doi.org/10.1016/0022-4073(82)90107-8

Gladstone, G. (1988). UV resonance line dayglow emissions on Earth and Jupiter. *Journal of Geophysical Research*, *93*(A12), 14,623–14,630.

Grebowsky, J., Benna, M., Plane, J. M. C., Collinson, G. A., Mahaffy, P. R., Jakosky, B. M., et al. (2017). Unique, non-Earthlike, meteoritic ion behavior in the upper atmosphere of Mars. *Geophysical Research Letters*, *44*, 3066–3072. https://doi.org/10.1002/2017GL072635

Grebowsky, J., Goldberg, R., & Pesnell, D. (1998). Do meteor showers significantly perturb the ionosphere? *Journal of Atmospheric and Solar: Terrestrial Physics*, *60*(6), 607–615. https://doi.org/10.1016/S1364-6826(98)00004-2

Gurnett, D., Morgan, D. D., Persoon, A. M., Granroth, L. J., Kopf, A. J., Plaut, J. J., et al. (2015). An ionized layer in the upper atmosphere of Mars caused by dust impacts from comet Siding Spring. *Geophysical Research Letters*, *42*, 4745–4751. https://doi.org/10.1002/2015GL063726

Jain, S., Stewart, A. I. F., Schneider, N. M., Deighan, J., Stiepen, A., Evans, J. S., et al. (2015). The structure and variability of Mars upper atmosphere as seen in MAVEN/IUVS dayglow observations. *Geophysical Research Letters*, *42*, 9023–9030. https://doi.org/10.1002/2015GL065419

Jakosky, B., Grebowsky, J. M., Luhmann, J. G., Connerney, J., Eparvier, F., Ergun, R., et al. (2015). MAVEN observations of the response of Mars to an interplanetary coronal mass ejection. *Science*, *350*(6261), aad0210. https://doi.org/10.1126/science.aad0210

Jakosky, B., Lin, R. P., Grebowsky, J. M., Luhmann, J. G., Mitchell, D. F., Beutelschies, G., et al. (2015). The Mars Atmosphere and Volatile Evolution (MAVEN) Mission. *Space Science Reviews*, *195*(1-4), 3–48. https://doi.org/10.1007/s11214-015-0139-x

Jakosky, B., Slipski, M., Benna, M., Mahaffy, P., Elrod, M., Yelle, R., et al. (2017). Mars' atmospheric history derived from upper-atmosphere measurements of 38Ar/36Ar. *Science*, *355*, 1409–1410.

Janches, D., Swarnalingam, N., Carrillo-Sanchez, J. D., Gomez-Martin, J. C., Marshall, R., Nesvorný, D., et al. (2017). Radar Detectability Studies of Slow and Small Zodiacal Dust Cloud Particles. III. The Role of Sodium and the Head Echo Size on the Probability of Detection. *The Astrophysical Journal*, *843*(1). https://doi.org/10.3847/1538-4357/aa775c

Kelleher, D. E., & Podobedova, L. I. (2008). Atomic transition probabilities of sodium and magnesium: A critical compilation. *Journal of Physical and Chemical Reference Data*, *37*(1), 267–706. https://doi.org/10.1063/1.2735328

Kelley, M. S. P., Farnham, T. L., Bodewits, D., Tricarico, P., & Farnocchia, D. (2014). A study of dust and gas at Mars from comet C/2013 A1 (Siding Spring). *The Astrophysical Journal Letters*, *792*(1), L16.

Kramida, A., Ralchenko, Y., Reader, J., & NIST ASD Team (2015). NIST atomic spectra database (ver. 5.3).

Leblanc, F., Chaufray, J. Y., Lilensten, J., Witasse, O., & Bertaux, J. L. (2006). Martian dayglow as seen by the SPICAM UV spectrograph on Mars express. *Journal of Geophysical Research*, *111*, E09S11. https://doi.org/10.1029/2005JE002664

Lillis, R. J., Halekas, J. S., Fillingim, M. O., Poppe, A. R., Collinson, G., Brain, D. A., & Mitchell, D. L. (2018). Field-aligned electrostatic potentials above the Martian exobase from MGS electron reflectometry: Structure and variability. *Journal of Geophysical Research: Planets*, *123*, 67–92 . https://doi.org/10.1002/2017JE005395

Lumpe, J. D., Bevilacqua, R. M., Hoppel, K. W., Krigman, S. S., Kriebel, D. L., Debrestian, D. J., et al. (1997). POAM II retrieval algorithm and error analysis. *Journal of Geophysical Research*, *102*(D19), 23,593–23,614. https://doi.org/10.1029/97JD00906

Lumpe, J. D., Bevilacqua, R. M., Hoppel, K. W., & Randall, C. E. (2002). POAM III retrieval algorithm and error analysis. *Journal of Geophysical Research*, *107*(D21), 4575. https://doi.org/10.1029/2002JD002137

Lumpe, J. D., Floyd, L. E., Herring, L. C., Gibson, S. T., & Lewis, B. R. (2007). Measurements of thermospheric molecular oxygen from the solar ultraviolet spectral irradiance monitor. *Journal of Geophysical Research*, *112*, D16308. https://doi.org/10.1029/2006JD008076

McClintock, B. (2014). *SORCE SOLSTICE FUV level 3 solar spectral irradiance daily means, version 013*. Greenbelt, MD: NASA Goddard Earth Sci. Data and Inf. Services Cent. (GES DISC).

McClintock, W., Schneider, N. M., Holsclaw, G. M., Clarke, J. T., Hoskins, A. C., Stewart, I., et al. (2015). The Imaging Ultraviolet Spectrograph (IUVS) for the MAVEN Mission. *Space Science Reviews*, *195*(1-4), 75–124. https://doi.org/10.1007/s11214-014-0098-7

McNaught, R. H., Sato, H., & Williams, G. V. (2013). Comet C/2013 A1 (Siding Spring). *Central Bureau Electronic Telegrams*, *3368*.

Molina-Cuberos, G., Witasse, O., Lebreton, J.-P., Rodrigo, R., López-Moreno, J. J., et al. (2003). Meteoric ions in the atmosphere of Mars. *Planetary and Space Science*, *51*(3), 239–249. https://doi.org/10.1016/S0032-0633(02)00197-6

Moorhead, A. V., Wiegert, P. A., & Cooke, W. J. (2014). The meteoroid fluence at Mars due to Comet C/2013 A1 (Siding Spring). *Icarus*, *231*, 13–21. https://doi.org/10.1016/j.icarus.2013.11.028

Pätzold, M., Tellmann, S., Häusler, B., Hinson, D., Schaa, R., & Tyler, G. L. (2005). A sporadic third layer in the ionosphere of Mars. *Science*, *310*(5749), 837–839. https://doi.org/10.1126/science.1117755

Plane, J. M. C. (1991). The chemistry of meteoric metals in the upper atmosphere. *International Reviews of Physical Chemistry*, *10*(1), 55–106. https://doi.org/10.1080/01442359109353254

Plane, J. M. C., Carrillo-Sanchez, J. D., Mangan, T. P., Crismani, M. M. J., Schneider, N. M., & Määttänen, A. (2018). Meteoric metal chemistry in the Martian atmosphere. *Journal of Geophysical Research: Planets*, *123*, 695–707. https://doi.org/10.1002/2017JE005510

Plane, J. M. C., Feng, W., & Dawkins, E. (2015). The mesosphere and metals: Chemistry and changes. *Chemical Reviews*, *115*(10), 4497–4541. https://doi.org/10.1021/cr500501m

Plane, J. M. C., Flynn, G. J., Määttänen, A., Moores, J. E., Poppe, A. R., Carrillo-Sanchez, J. D., & Listowski, C. (2018). Impacts of cosmic dust on planetary atmospheres and surfaces. *Space Science Reviews*, *214*(1), 214. https://doi.org/10.1007/s11214-017-0458-1

Rees, M. (1989). *Physics and chemistry of the upper atmosphere* (Vol. 1). Cambridge: Cambridge University Press. https://doi.org/10.1017/CBO9780511573118

Restano, M., Plaut, J. J., Campbell, B. A., Gim, Y., Nunes, D., Bernardini, F., et al. (2015). Effects of the passage of Comet C/2013 A1 (Siding Spring) observed by the Shallow Radar (SHARAD) on Mars Reconnaissance Orbiter. *Geophysical Research Letters*, *42*, 4663–4669. https://doi.org/10.1002/2015GL064150

Schneider, N., Deighan, J. I., Stewart, A. I. F., McClintock, W. E., Jain, S. K., Chaffin, M. S., et al. (2015). MAVEN IUVS observations of the aftermath of the Comet Siding Spring meteor shower on Mars. *Geophysical Research Letters*, *42*, 4755–4761. https://doi.org/10.1002/2015GL063863

Smith, P. L., Heise, C., Esmond, J. R., & Kurucz, R. L. (1995). *Atomic spectral line database [from CD-ROM 23 of R.L. Kurucz]*. Cambridge: Smithsonian Astrophysical Observatory.

Stevens, M., Evans, J. S., Schneider, N. M., Stewart, A. I. F., Deighan, J., Jain, S. K., et al. (2015). New observations of molecular nitrogen in the Martian upper atmosphere by IUVS on MAVEN. *Geophysical Research Letters*, *42*, 9050–9056. https://doi.org/10.1002/2015GL065319

Stevens, M. H., Gustin, J., Ajello, J. M., Evans, J. S., Meier, R. R., Kochenash, A. J., et al. (2011). The production of Titan's ultraviolet nitrogen airglow. *Journal of Geophysical Research*, *116*, A05304. https://doi.org/10.1029/2010JA016284

Strickland, D. J., Bishop, J., Evans, J. S., Majeed, T., Shen, P. M., Cox, R. J., et al. (1999). Atmospheric Ultraviolet Radiance Integrated Code (AURIC): Theory, software architecture, inputs, and selected results. *Journal of Quantitative Spectroscopy & Radiative Transfer*, *62*(6), 689–742. https://doi.org/10.1016/S0022-4073(98)00098-3

Tricarico, P., Samarasinha, N. H., Sykes, M. V., Li, J. Y., Farnham, T. L., Kelley, M. S. P., et al. (2014). Delivery of dust grains from comet C/2013 A1 (Siding Spring) to Mars. *The Astrophysical Journal Letters*, *787*(2), L35. https://doi.org/10.1088/2041-8205/787/2/L35

Vaubaillon, J., Maquet, L., & Soja, R. (2014). Meteor hurricane at Mars on 2014 October 19 from comet C/2013 A1. *Monthly Notices of the Royal Astronomical Society*, *439*(4), 3294–3299.

Vondrak, T., Plane, J. M. C., Broadley, S., & Janches, D. (2008). A chemical model of meteoric ablation. *Atmospheric Chemistry and Physics*, *8*(23), 7015–7031. https://doi.org/10.5194/acp-8-7015-2008

Whalley, C., & Plane, J. M. C. (2010). Meteoric ion layers in the Martian atmosphere. *Faraday Discussions*, *147*, 349–368. https://doi.org/10.1039/c003726e

Withers, P., Mendillo, M., Hinson, D. P., & Cahoy, K. (2008). Physical characteristics and occurrence rates of meteoric plasma layers detected in the Martian ionosphere by the Mars Global Surveyor Radio Science Experiment. *Journal of Geophysical Research*, *113*, A12314. https://doi.org/10.1029/2008JA013636